This is the accepted manuscript made available via CHORUS. The article has been published as:

# Renormalized quasiparticles, topological monopoles, and superconducting line nodes in heavy-fermion math xmlns="http://www.w3.org/1998/Math/MathML">mrow>mi>Ce/mi>mi>T/mi>msub>mi>X/mi>mn>3/mn>/msub>/mrow>/math> compounds

Vsevolod Ivanov, Xiangang Wan, and Sergey Y. Savrasov

Phys. Rev. B **103**, L041112 — Published 25 January 2021

DOI: 10.1103/PhysRevB.103.L041112

# Renormalized quasiparticles, topological monopoles and superconducting line nodes in heavy fermion $CeTX_3$ compounds

Vsevolod Ivanov,[1,*] Xiangang Wan,[2] and Sergey Y. Savrasov[1,†]

[1] *Department of Physics, University of California, Davis, California 95616, USA*
[2] *Department of Physics, Nanjing University, Nanjing 210093, China*

Non-centrosymmetric superconductors have recently attracted much attention, since the lack of inversion symmetry mixes spin singlet and triplet pairing states, which may allow the realization of topological superconductivity. In this work, we study the electronic properties of the family of inversion-broken $CeTX_3$ heavy-fermion superconductors, finding topological nodal lines as well as Dirac and Weyl points, which are renormalized closer to the Fermi energy by correlations. We find that the Weyl nodal lines have a substantial effect on the Fermi surface spin structure of the normal state, and lead to line nodes in the superconducting phase.

Superconductivity (SC) in non-centrosymmetric compounds has received much attention due to their potential for hosting unconventional pairing states. The lack of inversion symmetry permits antisymmetric spin-orbit coupling (ASOC) which splits the Fermi surface (FS) and mixes spin-singlet and spin-triplet SC pairing states.

The $CeTX_3$ (T = Co, Rh, Ir, X = Si, Ge) family of compounds crystallize in the $BaNiSn_3$-type structure ($I4mm$ space group no. 107), which breaks spatial inversion symmetry. With the exception of paramagnetic $CeCoSi_3$, their low-temperature phases are antiferromagnetic (AF) at ambient pressure. Application of pressure suppresses the Néel temperature to zero, where the magnetic ground state gives way to SC. The SC in this group exhibits many unconventional features, including upper critical fields $H_{cw}$ that far exceed the Pauli limiting field $H_p[T] \sim 1.86T_C[K]$[1–8] which has been suggested as evidence of an odd parity SC gap function. Recent works argue that AF fluctuations play a role in the development of SC, indicating the importance of the spin structure to the unconventional physics in these compounds.

The absence of inversion symmetry is also a necessary ingredient for the existence of topological Weyl points. Since the role of ASOC and lack of inversion symmetry in the development of the SC state is not well understood, we hope to shed some light by investigating the topological properties of these materials. Furthermore, the narrow Ce-$4f$ band is sensitive to temperature and pressure, allowing Weyl points to be tuned without introduction of chemical or site disorder. This feature makes these heavy fermion materials promising candidates for the study of Weyl physics [9] in the proximity of SC and quantum criticality.

Our electronic structure calculations are performed within the framework of the full potential linear muffintin orbital method with spin-orbit coupling, using the experimentally measured lattice parameters [10–13]. The compounds are locked to the paramagnetic state to mimic the experimentally observed suppression of magnetism by pressure. The on-site interactions between the Ce-$4f$ electrons must be treated with special care, as the strong Coulomb repulsion narrows the bandwidth considerably. We handle renormalization of quasiparticle bands through the LDA+Gutzwiller (LDA+G) method, taking Hubbard $U$ values of 5eV and 6eV[14]. The method is described in more detail in Refs. [15–19]

In LDA+G, the double-counting potential must carefully be chosen to account for the Coulomb correction included in both the single-particle and interacting terms of the Hamiltonian. Specifically, for the electron self-energy correction, $\Sigma_\alpha(0) - V_{\mathrm{DC},\alpha}$, there are several options for the double counting potential $V_{\mathrm{DC},\alpha}$ [15]. One such option is to set $V_{\mathrm{DC},\alpha} = \Sigma_\alpha(0)$, which leaves the LDA FS intact. Another option is to compute the crystal-field modifications self-consistently using an average over orbital self-energies, $V_{DC,\alpha} = \frac{1}{N}\sum_\alpha^N \Sigma_\alpha(0)$. For the $CeTX_3$ compounds, the crystalline electric field (CEF) effect of the tetragonal symmetry lifts the degeneracy of the J=5/2 total angular momentum state, splitting it into three doublets. Magnetic susceptibility and inelastic neutron scattering experiments [20–23] have determined the ground state doublet to be $\Gamma_7^{(1)}$ with $\Gamma_6$ and $\Gamma_7^{(2)}$ slightly higher in energy. Our LDA calculation shows that the lowest energy doublet hybridizes with the four bands crossing the Fermi energy ($E_F$), which are largely responsible for the shape of the FS. This is consistent with prior works that show qualitative agreement between the LDA FS and experimental de Haas-van Alphen measurements for $CeRhSi_3$ [13]. In order to best match the experimentally determined Fermi surfaces and mass enhancements we take a phenomenological approach, selecting a hybrid double counting scheme which independently treats the lowest energy doublets while the remaining states are shifted upward by 0.1Ry [24]. A different choice of shift parameter does not affect the states near the Fermi energy, and does not change the conclusions of our work. An analogous energy shift was used to find the FS of the isostructural $LaTX_3$, which is presumed to be very similar to that of the respective $CeTX_3$ compounds since their Ce-$4f$ electrons are highly localized [25, 26].

Our LDA+G procedure yields band-dependent quasiparticle residues $z_\alpha$, which are summarized in Table I. It is worth noting that the $\Gamma_7^{(2)}$ doublet has been determined to be the lowest lying state in $CeRhSi_3$ [26]. However, our calculations place the $\Gamma_7^{(1)}$ doublet at the lowest energy for all six isoelectronic compounds. The trends in the $CeTX_3$ series can be understood in terms of a Doniach phase diagram arising from competing RKKY and Kondo interactions [27]. The tuning parameter in the Doniach phase diagram is $|J_{cf}|N(0)$ where $J_{cf}$ is the magnetic exchange interaction and $N(0)$ is the density of states at the $E_F$. Experimentally, this parameter can be tuned by compressing the lattice using pressure, resulting in a greater hybridization of the conduction and Ce-4$f$ bands, thus decreasing the localization of the electrons. This is reflected directly in the trend of Néel temperatures, with $CeTGe_3$ compounds exceeding their Si counterparts, ($T_N$ = 21K, 14.6K, 8.7K vs. 0K, 1.8K, 5.0K for T = Co, Rh, Ir), due to their larger lattice constants [10]. The Néel temperatures of $CeRhSi_3$ and $CeIrSi_3$ are suppressed to zero at relatively low pressures $P_c \sim 2$ GPa, indicating their proximity to a quantum critical point.

The computed $z_\alpha$ values follow a decreasing trend with increasing lattice volumes, and qualitatively match the experimental trend of larger quasiparticle masses as the mass of the transition metal atom increases. These imply a factor of ∼2−9-fold increase in Sommerfield $\gamma$ values, but experimental measurements on $CeTX_3$ compounds in the high pressure paramagnetic state are not presently available for comparison.

The bands crossing $E_F$ are predominantly Ce-4$f$ in character, with a minor contribution from the transition metal $d$-orbitals away from the Fermi level. When Coulomb interactions are considered through the LDA+G calculation described above, their bandwidth is narrowed and the Fermi level is pinned to the lower doublet due to the increased density of states (Figure 1), changing the electronic structure and associated topological features near $E_F$. We emphasize that while the particular number and shape of the topological features depend on the choice of double counting potential and magnitude of Hubbard-$U$, their existence is guaranteed by symmetry and robust to correlations. Since the $CeTX_3$ compounds are isoelectronic, the general picture of their topological properties is the same, with each compound hosting different sets of particular features based on the relative band positions determined by the CEF splitting. For the remainder of this work we will focus on describing the electronic properties of $CeCoGe_3$, which hosts representative members of each type of topological features found in the series, including Dirac points (DPs) [28–33], Weyl points (WPs) [34–37], and nodal lines (NLs) [38–41].

**TABLE I:** Quasiparticle residues $z_\alpha$ for the lowest energy states for the members of the $CeTX_3$ series.

| | $z_{\mathrm{LDA+G}}$ ($U$=5 eV) | | | $z_{\mathrm{LDA+G}}$ ($U$=6 eV) | | |
|---|---|---|---|---|---|---|
| | $\Gamma_7^{(1)}$ | $\Gamma_6$ | $\Gamma_7^{(2)}$ | $\Gamma_7^{(1)}$ | $\Gamma_6$ | $\Gamma_7^{(2)}$ |
| $CeCoSi_3$ | 0.59 | 0.57 | 0.87 | 0.54 | 0.52 | 0.82 |
| $CeRhSi_3$ | 0.43 | 0.41 | 0.86 | 0.37 | 0.36 | 0.81 |
| $CeIrSi_3$ | 0.43 | 0.42 | 0.86 | 0.38 | 0.36 | 0.81 |
| $CeCoGe_3$ | 0.38 | 0.36 | 0.85 | 0.33 | 0.32 | 0.78 |
| $CeRhGe_3$ | 0.16 | 0.14 | 0.92 | 0.12 | 0.10 | 0.89 |
| $CeIrGe_3$ | 0.15 | 0.14 | 0.93 | 0.11 | 0.09 | 0.91 |

To locate and confirm the topological features, we use a one shot method for data mining the bands [42]. We divide the BZ into an initial 20 × 20 × 20 **k**-grid, computing the integral of Berry curvature fluxes through the surface of each k-cube to find sources and sinks. The locations of these topological points are recursively refined by repeating the procedure on a 4 × 4 × 4 grid within their **k**-cube until the desired precision is achieved, thus resolving much finer details of the material topology.

We find two classes of WPs in $CeCoGe_3$. The first appears in sets of eight confined to the $k_z = 0$ plane, while the second comes in sets of 16 which are additionally separated in the $k_z$ direction. Table II shows selected WPs of $CeCoGe_3$ listed along with their presumptive counterparts in LDA+G, which are shifted slightly in momentum space due to band renormalization. In total, $CeCoGe_3$ has seven (eight) non-equivalent Weyl points in LDA (LDA+G); additional details can be found in the Supplemental Material (SM) [24].

The most striking topological structure in the BZ is

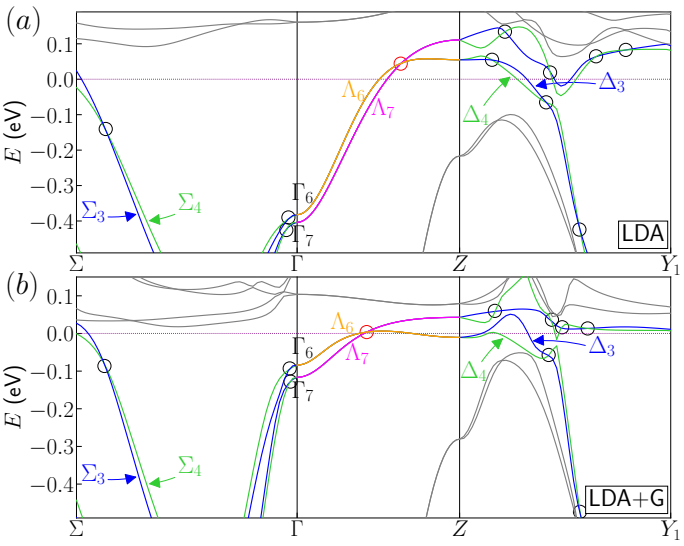



**FIG. 1:** Band structures for $CeCoGe_3$ using (a) LDA, and (b) LDA+G. Bands are labeled with their character representations according to their mirror eigenvalue: $\Sigma_3/\Delta_3$ (blue) for -$i$ and $\Sigma_4/\Delta_4$ (green) for $i$ within the mirror planes. Along the $\Gamma - Z$ line, doublets $\Lambda_6$ (orange) and $\Lambda_7$ (magenta) form a DP. NL crossings and DPs are indicated by black and red circles respectively.

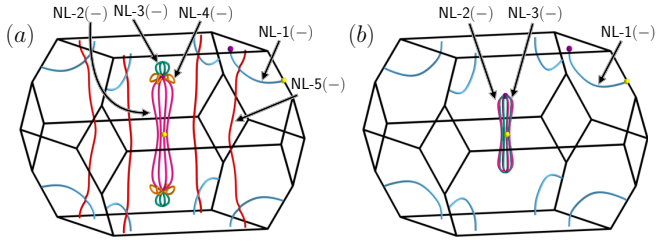



**FIG. 2:** Selected NLs in $CeCoGe_3$ for LDA (a), and LDA+G (b), with colored spheres showing start (yellow)/end (purple) points for NLs plotted in Fig. 3.

the set of nodal lines emerging from the Dirac point in this material. The band inversion mechanism generating the DP along the $\Gamma - Z$ axis is similar to that responsible for the DP in the inversion broken $Cd_3As_2$ [30], which shares the $C_{4v}$ point group symmetry. Along the $\Gamma - Z$ direction, compatibility relations for the double group connect $\Gamma_7 \rightarrow \Lambda_7$ and $\Gamma_6 \rightarrow \Lambda_6$. When moving along $\Gamma - Z$, the lowest lying $\Lambda_7$ Kramer's doublet switches with the $\Lambda_6$ doublet. The DP formed by the two doublets persists with the inclusion of band renormalizations, shifting from a position $k_z = 0.644\frac{2\pi}{c}$ in LDA to $k_z = 0.4285\frac{2\pi}{c}$ in LDA+G, closer to the $\Gamma$ point, as shown in Figure 1.

Moving away from the $\Gamma - Z$ axis within the $\sigma_v$ ($\sigma_d$) mirror plane, compatibility relations dictate that the $\Lambda_6$ and $\Lambda_7$ doublets split into bands with $\Sigma_3/\Sigma_4$ ($\Delta_3/\Delta_4$) irreducible representation. They can be distinguished by their mirror eigenvalue, with $-i$ corresponding to $\Sigma_3/\Delta_3$ and $+i$ to $\Sigma_4/\Delta_4$. Intersecting bands belonging to different mirror plane irreducible representations form a topologically protected continuous line of degeneracy called a Weyl nodal line [43]. Such NLs are protected by mirror symmetry, and are robust against perturbations. Verification of NL topology is further discussed in the SM[24].

A selection of NLs in $CeCoGe_3$ are shown in Figure 2. In LDA, three NLs emerge from the DP, with NL-2 and NL-3 forming loops within the $\sigma_v$ plane and NL-4 forming a loop in the $\sigma_d$ planes. The two other NLs within the $\sigma_d$ plane, NL-1 and NL-5, do not form loops, instead connecting across the edge of the BZ. When correlations are considered, the NL structure of $CeCoGe_3$ changes dramatically. NL-3 mixes with other NLs (not pictured), inverting to connect across the $k_z = 0$ plane, nearly coinciding with NL-2, while NL-4 and NL-5 are destroyed by correlations. On the other hand, the momentum-space structures of NL-1 and NL-2 do not change much in LDA+G. We note that since NL-3 and NL-4 are very small features and are strongly affected by correlations, it is unlikely that they can be resolved experimentally. The SM[24] contains the details of several additional NLs which lie farther from $E_F$, for a total of 15 (12) NLs in LDA (LDA+G).

**TABLE II:** Non-equivalent WPs of $CeCoGe_3$, with columns: topological charge (C), number of symmetry equivalent WP in this set (#), location ($\mathbf{k}_{\text{Weyl}}$) given in units of $(2\pi/a, 2\pi/a, 2\pi/c)$, and energy in meV (E). The Fermi energy is set to 0 eV.

| $CeCoGe_3$ | | LDA | | LDA+G | |
|---|---|---|---|---|---|
| C | # | $\mathbf{k}_{\text{Weyl}}$ | E | $\mathbf{k}_{\text{Weyl}}$ | E |
| +1 | 8 | (0.097, 0.187, 1.000) | -109 | (0.161, 0.133 , 1.000) | -49 |
| −1 | 16 | (0.118, 0.152, 0.556) | -140 | (0.131, 0.168 , 0.586) | -110 |
| +1 | 16 | (0.235, 0.271, 0.676) | +78 | (0.167, 0.236 , 0.530) | +33 |
| −1 | 16 | (0.057, 0.285, 0.996) | +118 | (0.083, 0.221 , 0.617) | +37 |

As we have mentioned previously, the renormalization of quasiparticle bands by correlations affects not only the momentum-space position of topological features, but also the energy at which they are located. Coulomb interactions substantially reduce the width of the Ce-4$f$ bands and pin them to the Fermi energy due to the increased density of states. A consequence of this renormalization is that any topological features formed by the Ce-4$f$ bands move closer to the $E_F$, becoming more relevant for the SC physics.

We illustrate this by showing the renormalization of the first WP in Table II as well as NL-1 and NL-2 (Figure 3). Since the two NLs are formed from bands with a large Ce-4$f$ component, the renormalization of these bands by correlations has a twofold effect, narrowing the energy dispersion of the NLs and move them closer to the $E_F$. Likewise, the Weyl point located at $(0.09700\frac{2\pi}{a}, 0.18704\frac{2\pi}{a}, 1.0\frac{2\pi}{c})$ is formed from bands that have primarily Ce-4$f$ character near this momentum. The correlations introduced by LDA+G raise the energy by 60 meV, and shift the Weyl point to a new momentum space position $(0.16138\frac{2\pi}{a}, 0.13255\frac{2\pi}{a}, 1.0\frac{2\pi}{c})$.

While SC in the $CeTX_3$ compounds has been studied extensively, the nature of the pairing state has not been settled. There are a number of good reviews on super-

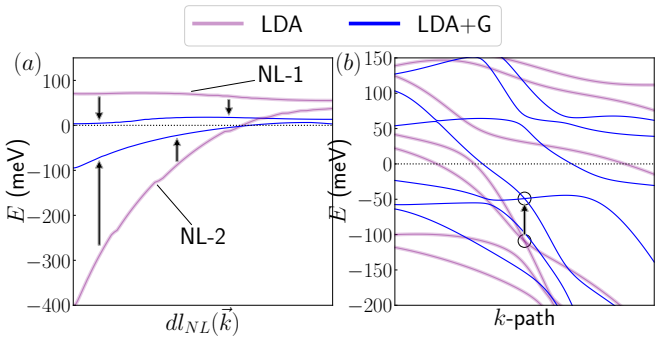



**FIG. 3:** Renormalization of topological features in $CeCoGe_3$ between LDA (violet) and LDA+G (blue). (a) Renormalization of NL-1 and NL-2. Energy is plotted along the length of each NL (normalized to unity), with start/end points as shown in Fig 2. (b) Plots of bands around the first WP from Table II. $k$-path is the straight line connecting $\mathbf{k}_{\text{Weyl}} \pm 0.1\hat{k}_y$.

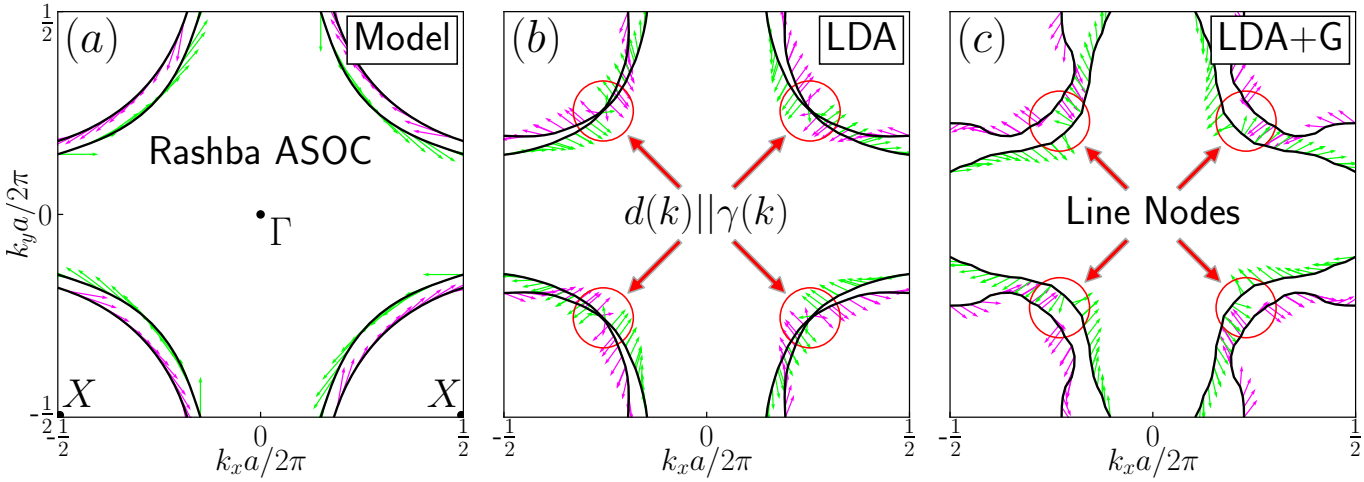



**FIG. 4:** Plots of the FS of $CeCoGe_3$ within the $k_z = 0$ plane for (a) the TB model, (b) LDA and (c) LDA+G. Green (magenta ) arrows show the direction of spins projected into the $xy-$plane for the upper (lower) band at each point. For LDA+G the energy is shifted by -5meV to avoid FS distortion due to pockets created by a set of Type-II Weyl points located just above $E_f$. Red circles highlight the spin distortion caused by the NLs in the normal state, which indicates the existence of zeros in $\boldsymbol{\gamma}(\mathbf{k})$ and implies line nodes in the SC gap function.

conductivity in non-centrosymmetric materials [44–47], which we will briefly outline here. The absence of inversion symmetry allows for an ASOC term,

$$H_{\mathrm{ASOC}} = \sum_{\mathbf{k}} \sum_{\alpha\beta=\uparrow,\downarrow} \boldsymbol{\gamma}(\mathbf{k}) \cdot \tilde{\boldsymbol{\sigma}}_{\alpha\beta} c^{\dagger}_{\mathbf{k}\alpha} c_{\mathbf{k}\beta}, \qquad (1)$$

where the Pauli matrices $\tilde{\boldsymbol{\sigma}} = (\tilde{\sigma}_x, \tilde{\sigma}_y, \tilde{\sigma}_z)$ act on the pseudospin basis states $|\mathbf{k}, \uparrow\rangle$ and $|\mathbf{k}, \downarrow\rangle$, and $c^{\dagger}_{\mathbf{k}\alpha}(c_{\mathbf{k}\beta})$ are the corresponding creation (annihilation) operators.

The form of $\boldsymbol{\gamma}(\mathbf{k})$ explicitly determines the local spin structure in $\mathbf{k}$-space. This places a constraint on the superconducting gap function $\Delta(k)$, which in general can be expanded in the basis of Pauli matrices as $\Delta(k) = [\psi(\mathbf{k}) + \mathbf{d}(\mathbf{k}) \cdot \tilde{\boldsymbol{\sigma}}] i\tilde{\sigma}_y$, with even-parity scalar $\psi(k)$ (singlet) and odd-parity vector $\mathbf{d}(\mathbf{k})$ (triplet) components. For sufficiently strong ASOC, $|\pm\mathbf{k}, \uparrow\rangle$ states become non-degenerate, which suppresses the component of $\mathbf{d}(\mathbf{k})$ that is not parallel to $\boldsymbol{\gamma}(\mathbf{k})$ [44, 45, 48, 49]. It then follows that the triplet component of the gap $\mathbf{d}(\mathbf{k})$ can be infered directly from the spin structure at the Fermi surface. The symmetry of the pairing gap has been studied in the context of anti-ferromagnetic spin-fluctuations near the SC transition [50, 51]. It has also been suggested that $CeRhSi_3$ and $CeIrSi_3$ may be topological Weyl superconductors [52, 53], and indeed our present study has identified a number Weyl nodes in the energy dispersion. However, the WPs found in our calculations are Type-II, with a hyperbolic FS that does not enclose the node. Their contribution to the FS topology is quite small, and most are too far away from $E_f$ to be relevant for the SC physics, even when taking band renormalization into account.

Instead we focus on the effect of topological NLs found in these compounds, which occupy a significantly larger phase space. Figure 4 shows cross sections of the $CeCoGe_3$ FS in the $k_z = 0$ plane for LDA and LDA+G, compared to a two band (TB) model (Figure 4a) which reproduces the principal FS features of the $CeTX_3$ family [50], showing a realignment of the spins beyond the usual Rashba-type ASOC due to the topological nodal lines near $E_F$. In LDA, the Type-II nodal line NL-5 passes through the $k_xk_y$-plane close to $E_F$, and its strongly tilted dispersion results in hyperboloid FS sheets around the $X$ point in Fig 4b. The spins along the surface rotate by an angle $\pi$ in the vicinity of the NL, creating a vortex-like defect which shrinks as the energy approaches the nodal line intersection. Exactly at the nodal line energy this vortex becomes vanishingly small, but the spin texture remains continuous due to the degeneracy of the bands. An animation of the spin rotations resulting from the nodal lines is included in the SM [24]. In LDA+G (Fig 4c), correlations shift the NL away from $E_F$, resulting in a gap between the Fermi surfaces, but leave the vortex-like spin defect unaffected. This spin distortion at the $\sigma_d$ planes is a direct consequence of the topological nature of the NLs, making it distinct from spin structures beyond Rashba ASOC which have been considered in other works [54–56].

It has been proposed that line nodes in the superconducting gap function could arise as a result of a topological defect in $\boldsymbol{\gamma}(\mathbf{k})$, and that such a state would be dominated by spin-triplet pairing and robust to perturbation[57]. The vortex-like defects in the spin structure that arise from the topological nodal lines in the normal state of $CeTX_3$ compounds can therefore serve as a natural origin for line nodes in the superconducting

gap. This result is consistent with experiments that have found evidence of gapless line-node superconductivity in $CeRhSi_3$ and $CeIrSi_3$ [8, 58–60]. Additional experiments are needed to clarify the form of the SC gap in this family of materials.

In summary, we have performed simulations of SC compounds in the $CeTX_3$ series with LDA and LDA+G, choosing the double counting potential in such a way that reproduces the experimental Fermi surfaces. We characterized the topological properties of their energy dispersion finding WPs and NLs, which are renormalized close to the $E_F$ by the strong Coulomb interactions of the Ce$-4f$ orbitals. These topological features in turn affect the spin-structure at the FS in these materials, which we have used to make a first-principles prediction of the superconducting gap structure.

This work was supported by NSF DMR Grant No. 1832728. X.G.W. acknowledges the support from NSFC 11834006 and the Tencent Foundation through the XPLORER PRIZE.

* E-mail: vivanov@ucdavis.edu
† E-mail: savrasov@physics.ucdavis.edu

[1] R. Settai, Y. Okuda, I. Sugitani, Y. nuki, T. D. Matsuda, Y. Haga, and H. Harima, International Journal of Modern Physics B **21**, 3238 (2007), https://doi.org/10.1142/S0217979207044287.
[2] N. Kimura, K. Ito, K. Saitoh, Y. Umeda, H. Aoki, and T. Terashima, Phys. Rev. Lett. **95**, 247004 (2005).
[3] F. Honda, I. Bonalde, K. Shimizu, S. Yoshiuchi, Y. Hirose, T. Nakamura, R. Settai, and Y. Ōnuki, Phys. Rev. B **81**, 140507 (2010).
[4] I. Sugitani, Y. Okuda, H. Shishido, T. Yamada, A. Thamizhavel, E. Yamamoto, T. D. Matsuda, Y. Haga, T. Takeuchi, R. Settai, and Y. nuki, Journal of the Physical Society of Japan **75**, 043703 (2006), https://doi.org/10.1143/JPSJ.75.043703.
[5] H. Wang, J. Guo, E. D. Bauer, V. A. Sidorov, H. Zhao, J. Zhang, Y. Zhou, Z. Wang, S. Cai, K. Yang, A. Li, X. Li, Y. Li, P. Sun, Y.-f. Yang, Q. Wu, T. Xiang, J. D. Thompson, and L. Sun, Phys. Rev. B **97**, 064514 (2018).
[6] T. Kawai, M. Nakashima, Y. Okuda, H. Shishido, T. Shimoda, T. D. Matsuda, Y. Haga, T. Takeuchi, M. Hedo, Y. Uwatoko, R. Settai, and Y. nuki, Journal of the Physical Society of Japan **76**, 166 (2007), https://doi.org/10.1143/JPSJS.76SA.166.
[7] R. Settai, Y. Miyauchi, T. Takeuchi, F. Lvy, I. Sheikin, and Y. nuki, Journal of the Physical Society of Japan **77**, 073705 (2008), https://doi.org/10.1143/JPSJ.77.073705.
[8] N. Kimura, K. Ito, H. Aoki, S. Uji, and T. Terashima, Phys. Rev. Lett. **98**, 197001 (2007).
[9] H.-H. Lai, S. E. Grefe, S. Paschen, and Q. Si, Proceedings of the National Academy of Sciences **115**, 93 (2018), https://www.pnas.org/content/115/1/93.full.pdf.
[10] T. Kawai, H. Muranaka, M.-A. Measson, T. Shimoda, Y. Doi, T. D. Matsuda, Y. Haga, G. Knebel, G. Lapertot, D. Aoki, J. Flouquet, T. Takeuchi, R. Settai, and Y. nuki, Journal of the Physical Society of Japan **77**, 064716 (2008), https://doi.org/10.1143/JPSJ.77.064716.
[11] A. D. Hillier, D. T. Adroja, P. Manuel, V. K. Anand, J. W. Taylor, K. A. McEwen, B. D. Rainford, and M. M. Koza, Phys. Rev. B **85**, 134405 (2012).
[12] V. K. Pecharsky, O.-B. Hyun, and K. A. Gschneidner, Phys. Rev. B **47**, 11839 (1993).
[13] T. Terashima, M. Kimata, S. Uji, T. Sugawara, N. Kimura, H. Aoki, and H. Harima, Phys. Rev. B **78**, 205107 (2008).
[14] B. T. Thole, G. van der Laan, J. C. Fuggle, G. A. Sawatzky, R. C. Karnatak, and J.-M. Esteva, Phys. Rev. B **32**, 5107 (1985).
[15] R. Dong, X. Wan, X. Dai, and S. Y. Savrasov, Phys. Rev. B **89**, 165122 (2014).
[16] Y. X. Yao, C. Z. Wang, and K. M. Ho, Phys. Rev. B **83**, 245139 (2011).
[17] K. M. Ho, J. Schmalian, and C. Z. Wang, Phys. Rev. B **77**, 073101 (2008).
[18] X. Deng, X. Dai, and Z. Fang, EPL (Europhysics Letters) **83**, 37008 (2008).
[19] X. Deng, L. Wang, X. Dai, and Z. Fang, Phys. Rev. B **79**, 075114 (2009).
[20] A. D. Hillier, D. T. Adroja, P. Manuel, V. K. Anand, J. W. Taylor, K. A. McEwen, B. D. Rainford, and M. M. Koza, Phys. Rev. B **85**, 134405 (2012).
[21] Y. Okuda, Y. Miyauchi, Y. Ida, Y. Takeda, C. Tonohiro, Y. Oduchi, T. Yamada, N. Duc Dung, T. D. Matsuda, Y. Haga, T. Takeuchi, M. Hagiwara, K. Kindo, H. Harima, K. Sugiyama, R. Settai, and Y. nuki, Journal of the Physical Society of Japan **76**, 044708 (2007), https://doi.org/10.1143/JPSJ.76.044708.
[22] M. Smidman, D. T. Adroja, A. D. Hillier, L. C. Chapon, J. W. Taylor, V. K. Anand, R. P. Singh, M. R. Lees, E. A. Goremychkin, M. M. Koza, V. V. Krishnamurthy, D. M. Paul, and G. Balakrishnan, Phys. Rev. B **88**, 134416 (2013).
[23] V. K. Anand, A. D. Hillier, D. T. Adroja, D. D. Khalyavin, P. Manuel, G. Andre, S. Rols, and M. M. Koza, Phys. Rev. B **97**, 184422 (2018).
[24] See Supplemental Material at [URL will be inserted by publisher] for more calculation details and a video showing spin rotations near the topological nodal lines.
[25] A. Thamizhavel, H. Shishido, Y. Okuda, H. Harima, T. D. Matsuda, Y. Haga, R. Settai, and Y. nuki, Journal of the Physical Society of Japan **75**, 044711 (2006), https://doi.org/10.1143/JPSJ.75.044711.
[26] Y. Muro, M. Ishikawa, K. Hirota, Z. Hiroi, N. Takeda, N. Kimura, and H. Aoki, Journal of the Physical Society of Japan **76**, 033706 (2007), https://doi.org/10.1143/JPSJ.76.033706.
[27] S. Doniach, "Phase diagram for the kondo lattice," in *Valence Instabilities and Related Narrow-Band Phenomena*, edited by R. D. Parks (Springer US, Boston, MA, 1977) pp. 169–176.
[28] S. M. Young, S. Zaheer, J. C. Y. Teo, C. L. Kane, E. J. Mele, and A. M. Rappe, Phys. Rev. Lett. **108**, 140405 (2012).
[29] Z. Wang, Y. Sun, X.-Q. Chen, C. Franchini, G. Xu, H. Weng, X. Dai, and Z. Fang, Phys. Rev. B **85**, 195320 (2012).
[30] Z. Wang, H. Weng, Q. Wu, X. Dai, and Z. Fang, Phys. Rev. B **88**, 125427 (2013).
[31] B.-J. Yang and N. Nagaosa, Nature Communications **5**, 4898 (2014).
[32] Q. D. Gibson, L. M. Schoop, L. Muechler, L. S. Xie, M. Hirschberger, N. P. Ong, R. Car, and R. J. Cava,

Phys. Rev. B **91**, 205128 (2015).
[33] Y. Du, B. Wan, D. Wang, L. Sheng, C.-G. Duan, and X. Wan, Scientific Reports **5**, 14423 (2015).
[34] X. Wan, A. M. Turner, A. Vishwanath, and S. Y. Savrasov, Phys. Rev. B **83**, 205101 (2011).
[35] H. Weng, C. Fang, Z. Fang, B. A. Bernevig, and X. Dai, Phys. Rev. X **5**, 011029 (2015).
[36] S.-M. Huang, S.-Y. Xu, I. Belopolski, C.-C. Lee, G. Chang, B. Wang, N. Alidoust, G. Bian, M. Neupane, C. Zhang, S. Jia, A. Bansil, H. Lin, and M. Z. Hasan, Nature Communications **6**, 7373 (2015).
[37] A. A. Soluyanov, D. Gresch, Z. Wang, Q. Wu, M. Troyer, X. Dai, and B. A. Bernevig, Nature **527**, 495 (2015).
[38] A. A. Burkov, M. D. Hook, and L. Balents, Phys. Rev. B **84**, 235126 (2011).
[39] R. Yu, H. Weng, Z. Fang, X. Dai, and X. Hu, Phys. Rev. Lett. **115**, 036807 (2015).
[40] Y. Kim, B. J. Wieder, C. L. Kane, and A. M. Rappe, Phys. Rev. Lett. **115**, 036806 (2015).
[41] Y. Du, F. Tang, D. Wang, L. Sheng, E.-j. Kan, C.-G. Duan, S. Y. Savrasov, and X. Wan, npj Quantum Materials **2**, 3 (2017).
[42] V. Ivanov and S. Y. Savrasov, Phys. Rev. B **99**, 125124 (2019).
[43] C. Fang, H. Weng, X. Dai, and Z. Fang, Chinese Physics B **25**, 117106 (2016).
[44] E. Bauer and M. Sigrist, *Non-Centrosymmetric Superconductors* (Springer, Berlin, Heidelberg, 2012).
[45] M. Smidman, M. B. Salamon, H. Q. Yuan, and D. F. Agterberg, Reports on Progress in Physics **80**, 036501 (2017).
[46] S. Yip, Annual Review of Condensed Matter Physics **5**, 15 (2014), https://doi.org/10.1146/annurev-conmatphys-031113-133912.
[47] F. Kneidinger, E. Bauer, I. Zeiringer, P. Rogl, C. Blaas-Schenner, D. Reith, and R. Podloucky, Physica C: Superconductivity and its Applications **514**, 388 (2015), superconducting Materials: Conventional, Unconventional and Undetermined.
[48] P. A. Frigeri, D. F. Agterberg, A. Koga, and M. Sigrist, Phys. Rev. Lett. **92**, 097001 (2004).
[49] K. V. Samokhin and V. P. Mineev, Phys. Rev. B **77**, 104520 (2008).
[50] Y. Tada, N. Kawakami, and S. Fujimoto, Journal of the Physical Society of Japan **77**, 054707 (2008), https://doi.org/10.1143/JPSJ.77.054707.
[51] Y. Tada, N. Kawakami, and S. Fujimoto, Phys. Rev. B **81**, 104506 (2010).
[52] A. Daido and Y. Yanase, Phys. Rev. B **94**, 054519 (2016).
[53] T. Yoshida and Y. Yanase, Phys. Rev. B **93**, 054504 (2016).
[54] Z. Zhong, A. Tóth, and K. Held, Phys. Rev. B **87**, 161102 (2013).
[55] D. Y. Usachov, I. A. Nechaev, G. Poelchen, M. Güttler, E. E. Krasovskii, S. Schulz, A. Generalov, K. Kliemt, A. Kraiker, C. Krellner, K. Kummer, S. Danzenbächer, C. Laubschat, A. P. Weber, J. Sánchez-Barriga, E. V. Chulkov, A. F. Santander-Syro, T. Imai, K. Miyamoto, T. Okuda, and D. V. Vyalikh, Phys. Rev. Lett. **124**, 237202 (2020).
[56] R. Moriya, K. Sawano, Y. Hoshi, S. Masubuchi, Y. Shiraki, A. Wild, C. Neumann, G. Abstreiter, D. Bougeard, T. Koga, and T. Machida, Phys. Rev. Lett. **113**, 086601 (2014).
[57] Y. Yanase and M. Sigrist, Journal of the Physical Society of Japan **77**, 124711 (2008), https://doi.org/10.1143/JPSJ.77.124711.
[58] H. Mukuda, T. Fujii, T. Ohara, A. Harada, M. Yashima, Y. Kitaoka, Y. Okuda, R. Settai, and Y. Onuki, Phys. Rev. Lett. **100**, 107003 (2008).
[59] H. Mukuda, T. Ohara, M. Yashima, Y. Kitaoka, R. Settai, Y. Ōnuki, K. M. Itoh, and E. E. Haller, Phys. Rev. Lett. **104**, 017002 (2010).
[60] J. F. Landaeta, D. Subero, D. Catalá, S. V. Taylor, N. Kimura, R. Settai, Y. Ōnuki, M. Sigrist, and I. Bonalde, Phys. Rev. B **97**, 104513 (2018).